Light-matter interactions in van der Waals photodiodes from first principles

Jiang Cao [ORCID],[*] Sara Fiore [ORCID],[*] Cedric Klinkert, Nicolas Vetsch, and Mathieu Luisier[†]
Integrated Systems Laboratory, ETH Zürich, 8092 Zurich, Switzerland

Strong light-matter interactions in van der Waals heterostructures (vdWHs) made of two-dimensional (2D) transition metal dichalcogenides (TMDs) provide a fertile ground for optoelectronic applications. Of particular interest are photoexcited interlayer electron-hole pairs, where electrons and holes are localized in different monolayers. Here, we present an *ab initio* quantum transport framework relying on maximally localized Wannier functions and the nonequilibrium Green's functions to explore light-matter interactions and charge transport in 2D vdWHs from first principles. Electron-photon scattering is accurately taken into account through dedicated self-energies. As testbed, the behavior of a $MoSe_2$-WSe_2 PIN photodiode is investigated under the influence of a monochromatic electromagnetic signal. Interlayer electron-hole pair generations are observed even in the absence of phonon-assisted processes. The origin of this phenomenon is identified as the delocalization of one valence band state over both monolayers composing the vdWH.

I. INTRODUCTION

An intriguing feature of van der Waals heterostructures (vdWHs) based on two-dimensional (2D) transition metal dichalcogenides (TMDs) is their ability to give rise to type-II band alignments, i.e., the conduction band minimum of the whole system is situated in one material, while its valence band maximum is located in another one. As a consequence, electrons and holes are confined in different layers. This, combined with the small interlayer spatial separation of vd-WHs, leads to strong electron-hole Coulomb interactions with large binding energies. As a consequence, spatially separated electron-hole pairs called interlayer excitons (IXs) can be created [1–3]. It is interesting to note that the spatial separation of the carriers induces a permanent electrical dipole moment aligned with the out-of-plane direction. Through this dipole, it is possible to control the electrical and optical properties of vdWHs [4,5]. Due to the spatial distribution of IX, a reduced overlap of the electron and hole wave function is observed as compared to their intralayer counterparts. Hence, the lifetime of IXs can reach hundreds of nanoseconds and beyond [6–8]. Moreover, it has been shown that the lifetime of IX can be modulated either by applying an external electric field [8,9], changing the interlayer distance [10,11], modifying the temperature at which the system operates [4,12], encapsulating the vdWH with hBN [13,14].

The extremely long lifetime of IXs allows them to more easily dissociate into free charge carriers (electrons and holes residing in different TMD monolayers) prior to their recombination. Photocurrent generation has been observed experimentally in $MoSe_2$-WSe_2 and MoS_2-WSe_2 vdWHs [15–17]. Fascinating many-body effects such as

Bose-Einstein condensation [18] and exciton transport [19] have been reported in such structures. Compared to coupled double quantum well systems [18,20,21] that can also host spatially indirect excitons, IXs in vdWHs possess unique properties that result from the vdW coupling and the enhanced Coulomb interactions present in 2D materials. The weak coupling between 2D monolayers enable various stacking orders, relative slidings [22], and twisting angles [23].

The physical mechanism behind the formation of IXs in vdWHs continues to be an active research area [24]. Photoluminesence (PL) excitation spectroscopy shows an enhanced IX intensity when the exciting light signal corresponds to the intralayer exciton energy [2,25]. Intuitively, one would expect inhibited interlayer charge transfers between different TMDs as a consequence of the weak out-of-plane coupling and the type-II band alignment [26–29]. However, experimental measurements revealed that ultrafast interlayer charge transfers occur in TMD-based heterostructure [30–33]. Such observations have been theoretically confirmed in Ref. [34] via time-dependent *ab initio* nonadiabatic molecular dynamics. In this study, it was proved that ultrafast interlayer charge transfer processes are promoted by specific phonons, which lead to carrier relaxations from one layer to the other. Here, through accurate device simulations it will be demonstrated that electron-hole pairs can also be created without the help of phonons. However, the probability and magnitude of the latter processes strongly depend on the band structure characteristics of the considered heterobilayer, which are sensitive to the stacking order and twisting angle of the monolayers.

Theoretical studies on light-matter interactions in optoelectronic nanodevices are usually carried out with model Hamiltonians relying on the effective mass approximation [35–37], $k \cdot p$ method [38], or tight-binding framework [39,40] with empirical parameters as inputs in all cases. Such models are ideal to validate methodological developments or to investigate quantum well structures made of conventional

---

[*]These authors contributed equally to this work.
[†]Corresponding author: mluisier@iis.ee.ethz.ch

semiconductors, e.g., GaAs or Si [41–44] and carbon nanotubes [39,40]. However, they are not suitable to examine heterobilayers of 2D materials that approach the ultimate atomic thickness and exhibit complex band structure, interlayer coupling, and electron-photon coupling matrix elements, whose features are unknown. On the other hand, *ab initio* calculations based on density functional theory (DFT) capture the full electronic band dispersion of heterobilayer, they automatically include the coupling between 2D monolayers, and they can provide electron-photon interactions from first principles [45–48]. Nevertheless, DFT calculations are typically performed assuming periodic boundary conditions in representative supercells that are kept at equilibrium with their environment. Such situations differ from those encountered in PIN vdWHs to which a voltage is applied: the periodicity is broken and an out-of-equilibrium current starts to flow. Hence, to predict the performance of 2D heterobilayer photodiodes and to shed light on the underlying physical processes, an advanced *ab initio* quantum transport tool is needed. One possibility to satisfy these requirements consists of combining density functional theory with the nonequilibrium Green's function (NEGF) formalism [49–51] and to include electron-photon interactions through scattering self-energies.

In this work, we introduce a DFT + NEGF approach for optoelectronic device simulations, in particular those concerned with vdWHs of TMD layers. As basis set, maximally localized Wannier functions (MLWFs) are used because of their limited extension in space [52]. First, an expression for the electron-photon scattering self-energy is derived in a localized basis set. Because carrier-carrier interactions are not included due to their high computational burden, our approach cannot describe excitons as quasiparticles. Still it captures the generation of electron-hole pairs resulting from the application of an optical signal and the subsequent separation of these carriers caused by the built-in potential. We showcase the developed methodology by analyzing a $MoSe_2$-WSe_2 heterobilayer PIN photodiode, as shown in Fig. 1, with two stacking orders, AA and AA'. The main finding of this work is that interlayer electron-hole pairs can be created via hybridized (delocalized) wave functions extending across both monolayers, without phonon-assisted interlayer transfers. This wave-function delocalization depends on the stacking order of the heterobilayer. We will also show that the nonlocal character of electron-photon interactions calls for the inclusion of long-range interactions in the quantum transport simulations.

This paper is organized as follows. In Section II the modeling framework and the equations for transport as well as for light-matter interactions are presented. The details of the *ab initio* calculations and the device specifics are described in Section III. Section IV is devoted to the presentation, analysis, and discussion of the device simulation results when an electromagnetic source is shined on a PIN photodiode made of a $MoSe_2$-WSe_2 vdWH. Finally, conclusions are drawn in Section V.

II. THEORY

The quantum transport equations at the core of our device simulations are solved using the nonequilibrium Green's
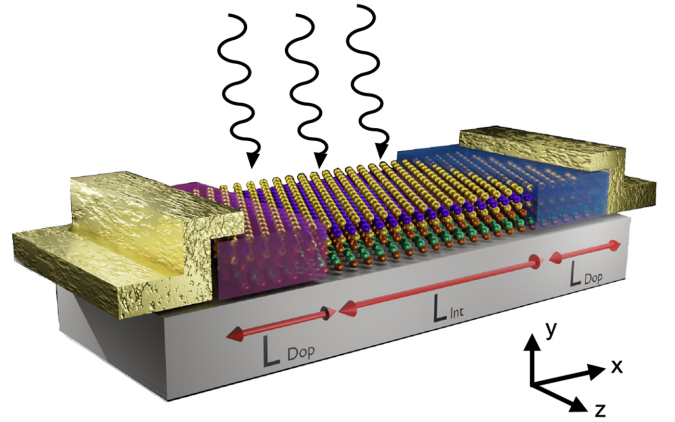

FIG. 1. Schematic view of a vdWH PIN photodiode with a vertically incident, linearly polarized optical signal. The N-doped (P-doped) region of length $L_{dop} = 10$ nm is represented by the blue (red) shaded box. The parameter L_{int} indicates the length of the intrinsic region and is equal to 40 nm as well. The yellow and purple (orange and green) spheres represent the Mo and Se (W and Se) atoms, respectively. Transport is aligned with the *x* axis, while *z* is assumed to be periodic. The simulation domain includes 2496 atoms in total.

function formalism [51]. All computations have been carried out with an in-house tool named OMEN that has been extensively tested [53–55]. It relies on self-consistent solutions of the Schrödinger and Poisson equations in 1D, 2D, and 3D geometries. For electrons, the following system of equations is solved:

$$(E \cdot I - H(k_z) - \Sigma^R(E, k_z)) \cdot G^R(E, k_z) = I, \quad (1)$$

$$G^{\gtrless}(E, k_z) = G^R(E, k_z) \cdot \Sigma^{\gtrless}(E, k_z) \cdot G^A(E, k_z), \quad (2)$$

where I is the identity matrix, E the electron energy, k_z the electron momentum along the direction(s) assumed periodic (*z* in Fig. 1), and $H(k_z)$ the Hamiltonian matrix (see Appendix). The G^R, $G^A = (G^R)^\dagger$, $G^<$, and $G^>$ quantities are the retarded, advanced, lesser, and greater Green's functions, respectively. The symbol $\dagger$ indicates the Hermitian transposition. The size of all matrices in Eqs. (1) and (2) is $N_O \times N_O$, where N_O is the total number of localized orbitals in the considered device. The $\Sigma^{R,\gtrless}$ self-energy matrices contain a boundary $\Sigma^{R,\gtrless B}$ and electron-photon scattering $\Sigma^{R,\gtrless S}$ term. The former connects the simulation domain to two semi-infinite left and right leads. It can be efficiently computed through contour integral techniques [56].

To compute the relevant entries of the Green's function matrices, the selected inversion (SINV) algorithm [57] implemented in the PARDISO library [58] was used in this work. It produces all G^R entries that correspond to the nonzero elements of the $H(k_z) + \Sigma^R(E, k_z)$ matrix. The same is obtained for $G^{\gtrless}$ based on the sparsity pattern of $\Sigma^{\gtrless}$. The advantage of SINV over, for example, the recursive Green's function (RGF) algorithm [59] is that the off-diagonal entries of G^R and $G^{\gtrless}$ can be calculated at a lower computational cost.

Taking into account the impact of an electromagnetic field translates into the following scattering self-energy expression:

$$
\begin{aligned}
\Sigma_{nm}^{\lessgtr,S}(E, k_z) = &\sum_{\lambda, l_1, l_2} \sum_{\vec{q}} \frac{e^2 \hbar^2}{2 V \epsilon_0 E_{ph,\lambda} m_0^2} [\vec{e}_{\vec{q}\lambda} \cdot \vec{p}_{nl_1}(k_z)] \\
&\times \left[N_{\vec{q},\lambda} G_{l_1 l_2}^{\lessgtr} \left(E \mp E_{ph,\lambda}, k_z - q_z \right) \right. \\
&\left. + (N_{\vec{q},\lambda} + 1) G_{l_1 l_2}^{\lessgtr} \left(E \pm E_{ph,\lambda}, k_z - q_z \right) \right] \\
&\times [\vec{e}_{\vec{q}\lambda} \cdot \vec{p}_{l_2 m}(k_z - q_z)],
\end{aligned}
\tag{3}
$$

where e is the electron charge, c_0 the speed of light, ϵ_0 the vacuum permittivity, m_0 the rest mass of electron, V the volume of the box that contains one period of the electromagnetic field, $\vec{e}_{\vec{q}\lambda}$ a unit vector aligned with the light polarization, $N_{\vec{q},\lambda}$ the Bose-Einstein distribution of the photon mode λ, q_z the z component of the photon momentum vector $\vec{q}$, and $\hbar$ the reduced Plank constant. The photon energy $E_{ph,\lambda}$ is equal to $\hbar\omega_\lambda$, where ω_λ is the frequency of the photon mode λ. The indices n, m, l_1, and l_2 run over all possible localized orbitals in the simulation domain. The momentum operator $\vec{p}_{nm}$ in real space can be computed as the commutator between the Hamiltonian operator and the position operator $\vec{r}$ that must be evaluated in the same localized basis,

$$
\vec{p}_{nm}(\vec{R}) = \frac{i m_0}{\hbar} \langle \vec{R}, n | [H, \vec{r}] | \vec{0}, m \rangle,
\tag{4}
$$

where $\vec{R}$ is a lattice vector connecting the unit cell located at the origin $\vec{0}$ to its periodic replica at $\vec{R}$, i is the imaginary unit, whereas the indices n and m run over all localized orbitals in each unit cell. By expanding Eq. (4), we obtain

$$
\vec{p}_{nm}(\vec{R}) = \frac{i m_0}{\hbar} \sum_{\vec{R}'l} \left[H_{nl}(\vec{R} - \vec{R}') \vec{r}_{lm}(\vec{R}') - \vec{r}_{nl}(\vec{R} - \vec{R}') H_{lm}(\vec{R}') \right].
\tag{5}
$$

Since $\vec{p}_{nm}(\vec{R})$ is a lattice periodic operator, it is diagonal in the wave vector $\vec{k}$ basis and can thus be expressed in $\vec{k}$ space as

$$
\vec{p}_{nm}(\vec{k}) = \sum_{\vec{R}} e^{i \vec{k} \cdot \vec{R}} \vec{p}_{nm}(\vec{R}).
\tag{6}
$$

A more extensive treatment of the momentum operator both in real and reciprocal space can be found in Ref. [60]. Important is that it is computed at the *ab initio* level using the same DFT inputs as for the Hamiltonian matrix.

Under the approximation that $N_{\vec{q},\lambda} \gg 1$, the spontaneous emission term in Eq. (3) can be neglected and the number of photons is assumed to be proportional to the energy density of the incident optical signal

$$
J_{\vec{q}\lambda} = \frac{c_0}{V} N_{\vec{q},\lambda} E_{ph,\lambda}.
\tag{7}
$$

In our simulations, light enters the 2D vdWHs orthogonal to their surface, as illustrated in Fig. 1. Furthermore, the photon momentum $\vec{q}$ is neglected due to its small magnitude as compared to the electron one so that Eq. (3) can be

simplified to

$$
\begin{aligned}
\Sigma_{nm}^{\lessgtr,S}(E, k_z) = &\sum_{\lambda, l_1, l_2} \frac{J_\lambda}{E_{ph,\lambda}^2} M_{nl_1}^\lambda(k_z) \\
&\times [G_{l_1 l_2}^{\lessgtr}(E \mp E_{ph,\lambda}, k_z) \\
&+ G_{l_1 l_2}^{\lessgtr}(E \pm E_{ph,\lambda}, k_z)] M_{l_1 m}^\lambda(k_z).
\end{aligned}
\tag{8}
$$

The electron-photon coupling matrix elements $M_{nm}^\lambda(k_z)$ are defined as

$$
M_{nm}^\lambda(k_z) = c_0 \vec{e}_{\vec{q}\lambda} \cdot \vec{p}_{nm}(k_z).
\tag{9}
$$

Note that all matrix blocks in Eq. (8), that is $\Sigma_{nm}^{\gtrless,S}$, $G_{nm}^{\gtrless}$, and M_{nm}^λ, have the same dimensions, $N_{\mathrm{orb},n} \times N_{\mathrm{orb},m}$, where $N_{\mathrm{orb},n/m}$ is the number of localized orbitals centered at position $\vec{R}_{n/m}$.

Contrary to other scattering mechanisms such as electron-phonon, light-matter interactions extend over long distances so that the self-energy in Eq. (8) cannot be reduced to its diagonal entries [61]. At the same time, considering full self-energy matrices is not possible from a computational point of view. We therefore introduced a cutoff radius r_{cut} that determines the largest possible interatomic interaction range. If the distance between atoms m and n, i.e., $|\vec{R}_m - \vec{R}_n|$ is larger than r_{cut}, then $G_{nm}^{\lessgtr}$, M_{nm}^λ, and $\Sigma_{nm}^{\lessgtr}$ in Eq. (8) are all set to 0. The influence of r_{cut} on the transport calculation results will be carefully analysed in Sec. III C.

Finally, the photoexcited current flowing through the vdWH devices can be computed with the following equation [62]:

$$
\begin{aligned}
I_d = \frac{2e}{\hbar} \sum_{k_z} \sum_{n,m} \int \frac{dE}{2\pi} \mathrm{tr}(&H_{nm}(k_z) \cdot G_{mn}^<(E, k_z) \\
&- G_{nm}^<(E, k_z) \cdot H_{mn}(k_z)).
\end{aligned}
\tag{10}
$$

Here, the indices m and n run over all orbitals situated within two consecutive transport cells. Spin is included through the prefactor 2 in Eq. (10).

Excitonic effects have a significant impact on the optical and optoelectronic properties of devices based on TMDCs. However, including such effects into an *ab initio* quantum transport framework goes beyond existing modeling capabilities due to the high computational burden associated with the treatment of many-body phenomena. A qualitative analysis of excitonic effects is provided in Sec. IV E.

III. COMPUTATIONAL DETAILS

A. DFT calculations

A MoSe$_2$-WSe$_2$ van der Waals heterostructure is investigated to illustrate the developed simulation approach and study interlayer electron-hole pair generations. The chosen stacking order is AA', which belongs to the D$_{3d}$ point group, following the same notation as in Ref. [63]. This configuration has been proved to be the one with the lowest energy [1,63–65].

The DFT package VASP [66,67] was employed to perform the required *ab initio* calculations for the primitive unit cell of the vdWH using the generalized gradient approxima-

tion (GGA) of Perdew, Burke, and Ernzerhof (PBE) [68], a Γ-centered Monkhorst-Pack k-point grid of dimension $21 \times 1 \times 21$ and a plane-wave cutoff energy of 600 eV. The DFT-D3 method of Grimme [69] accounts for the van der Waals interactions. For the forces acting on each ion, a convergence criterion smaller than 10^{-8} eV/Å was applied, while a total energy difference smaller than 10^{-10} eV between two subsequent iterations was set as the target. Along the stacking direction (c axis), aligned with the y axis of the device in Fig. 1, a large vacuum of 30 Å was placed to avoid spurious dipole interactions between the unit cell of interest and its periodic replica in the out-of-plane direction [70]. For the sake of simplicity, spin-orbit coupling (SOC) was neglected in our calculations, but we analyze its effects and discuss its impact on the results in Sec. IV C.

B. Quantum transport simulations

To determine the quantum transport properties of the device, it is more convenient to use a localized basis set. It facilitates the separation of the investigated domain into a central region and two contact regions and allows to model different device geometries. Therefore the plane-wave (PW) Hamiltonian obtained from VASP was transformed into a basis of maximally localized Wannier functions employing the WANNIER90 tool [52]. To provide an accurate description of the MoSe$_2$-WSe$_2$ band structure around its band gap, we used as initial projections five d-like orbitals per Mo and W atom and three p-like orbitals per Se atoms. With this setting, the MLWF band structure differs from the PW one around the conduction and valence band edges by no more than 10 meV.

By applying the upscale technique of Ref. [71] on the hexagonal unit cell of the MoSe$_2$-WSe$_2$ heterostructure, we constructed the simulation domain corresponding to the geometry in Fig. 1. For device calculations, an orthorhombic transport cell was employed and derived from the hexagonal unit cell by applying a transformation matrix of ((2, 0, 2), (0, 1, 0), (−2, 0, 2)) to its lattice vectors. The resulting transport cell has dimensions $a = 1.15$ nm (aligned with the transport direction x) and $b = 0.66$ nm (aligned with the periodic direction z, which is orthogonal to a). The final MoSe$_2$-WSe$_2$ PIN junction used to investigate light-matter interactions in vdWHs is presented in Fig. 1. It is made of 2496 atoms in total. The P- and N-doped regions measure L_{Dop}=10 nm each, while the central intrinsic region is of length L_{Int}=40 nm. A monochromatic, vertically incident, and x-polarized light is shined over the entire device from the top. Its energy density J in Eq. (7) is equal to 10^{10} W/m^2, a value much larger than in experiments (10^3 W/m^2) [72]. A high energy density is required to ensure that the magnitude of the photoexcited current remains above the numerical noise associated with the SINV or RGF algorithms. This must be done because the scattering electron-photon self-energy in Eq. (8) is directly proportional to the energy density of the incident light and typically orders of magnitude smaller than the Hamiltonian entries. Increasing J in Eq. (7) has however little influence on the results, the photocurrent depending linearly on this parameter, as shown in Fig. 2.

The simulation workflow proceeds as follows: first, Poisson's equation is self-consistently solved with the NEGF
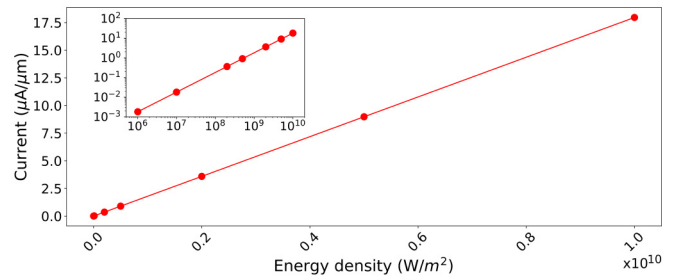

FIG. 2. Photocurrent extracted from the vdWH PIN photodiode in Fig. 1 as a function of the energy density J of the incident light. The photoenergy is set to 2.1 eV, while the built-in potential of the diode is equal to 0.4 V. The inset is a log-log plot of the results to better visualize the very low energy densities.

system in the ballistic limit of transport. The resulting electric potential, flat in the P and N regions and with a quasilinear potential drop in the intrinsic region, is then passed as an input to the dissipative quantum transport simulations with the electron-photon interactions activated. Upon illumination by a polarized light beam over the whole device region, a photocurrent is induced in the MoSe$_2$-WSe$_2$ PIN junction. Due to the very demanding computational burden associated with the resolution of the electro-optical transport problem, only one k_z point, the one corresponding to the K point in the Brillouin zone, was considered in this work. The energy vector E over which the Green's functions and self-energies are evaluated is homogeneously discretized with an interval of 0.02 eV. Although large this energy discretization is sufficient to capture the features of the generated photocurrents, as will be shown in the Result section.

C. Electron-photon scattering self-energies

As a first step, we investigated the influence of the cutoff radius, r_{cut}, which is applied to the Green's functions, scattering self-energies, and optical matrix elements, on the magnitude of the photoexcited current for the selected MoSe$_2$-WSe$_2$ PIN device. To do that, the vdWH was illuminated by a monochromatic light signal with an energy of 2.1 eV, while the built-in potential of the PIN diode was equal to 0.4 eV. The results are presented in Fig. 3(a). Performing such an analysis for this heterostructure is however very demanding. More than 15 days are required on 32 CPUs to include interactions up to $r_{\mathrm{cut}} = 2.29$ nm [see Fig. 3(b)]. For this reason, to be able to explore larger radii (up to 5.7 nm), we studied the influence of r_{cut} on the individual WSe$_2$ and MoSe$_2$ monolayers. No clear convergence of the photoexcited current can be observed, but its values remain within 10%–20% of the average taken over the entire r_{cut} range. Hence, adopting a relatively low r_{cut} value can be envisioned.

Furthermore, even if the absolute values of the optically induced current vary with r_{cut} its spectral and spatial distributions do not change much, as can be seen in Fig. 4, where the photocurrent density of a WSe$_2$ PIN diode is given as a function of the electron energy and its location along the transport direction x using a photon energy of 2.1 eV, for three different cutoff radii, $r_{\mathrm{cut}} = 1.1$, 3.4, and 5.5 nm. Similarly, in Fig. 5, the photocurrents corresponding
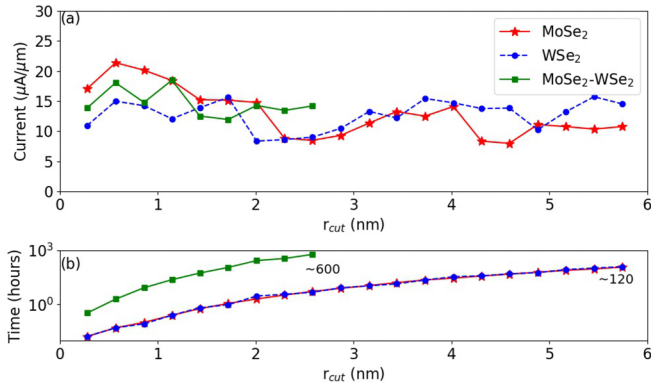
FIG. 3. (a) Optically induced electrical current in a 60-nm-long MoSe$_2$-WSe$_2$ (solid green line with squares), MoSe$_2$ (solid red line with stars), and WSe$_2$ (dashed blue line with dots) PIN photodiode as a function of the cutoff radius that limits the range of the entries in the scattering electron-photon self-energy in Eq. (8). The device is illuminated by a monochromatic light signal of energy 2.1 eV and the built-in potential is set to 0.4 V. (b) Time required to obtain the results in (a) with 128 CPUs for the individual monolayers and 32 CPUs for the vdWH. The approximate times in hours for the last points investigated are reported.

to $r_{cut} = 1.1$, 3.4, and 5.5 nm are plotted as a function of the electron energy at the position $x = 32.9$ nm along the transport direction, i.e., in the middle of the device. Clearly, the three curves qualitatively agree, thus justifying the usage of a small r_{cut}. To keep the computational burden manageable, the subsequent simulations of the MoSe$_2$-WSe$_2$ vdWH have been therefore carried out using $r_{cut} = 1$ nm, which is expected to provide qualitatively meaningful and quantitatively accurate (within 10%–20%) results. Our assumption is that the behavior of the photoexcited current in the MoSe$_2$-WSe$_2$ vdWH follows the same trend as that of the individual layers composing it.

IV. RESULTS AND DISCUSSION

A. Optical matrix elements

In Fig. 6(a), the electronic dispersion of the MoSe$_2$-WSe$_2$ vdWH projected onto the atomic orbitals of each TMD is presented. It is worth highlighting that the chosen TMD monolayers exhibit a direct band gap at the K point, but their AA' stacking leads to a slightly indirect band gap between the K and Γ point, which might prevent this material combination to be employed in high-efficiency optoelectronic applications. While the nature of the band gap (direct/indirect) can be controlled by fine tuning the atomic positions [73], introducing strain or changing the stacking might give rise to energetically less favourable configurations. Here, we decided to maintain the energetically most favourable stacking because the difference between the top valence band at Γ and its value at K does not exceed 0.13 eV.

The orbital character of each band significantly changes as a function of the momentum. At the K point, the lowest conduction band (CMB) belongs to MoSe$_2$, the highest valence band (VBM) to WSe$_2$. The second lowest conduction band (CMB + 1) comes from WSe$_2$, whereas the second highest
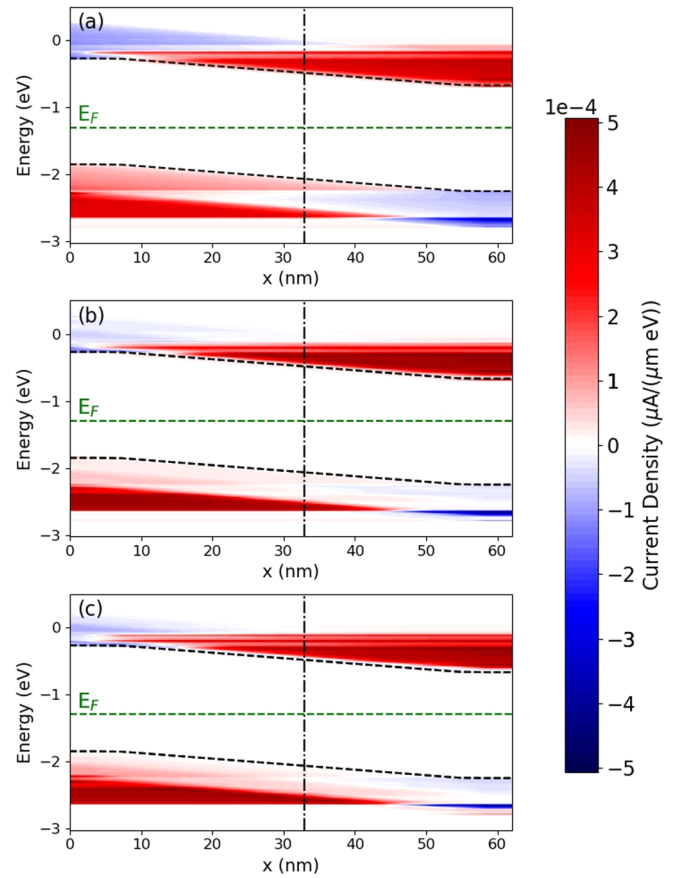

FIG. 4. (a) Spatial and spectral distribution of the optically induced current flowing through a WSe$_2$ PIN-junction using a cutoff radius $r_{cut} = 1.1$ nm, a monochromatic light illumination with energy $E_{ph} = 2.1$ eV, and a built-in potential of 0.4 eV. The Fermi level is indicated by the dashed green line. The conduction and valence band edges are represented by the dashed black lines. The black dashed and dotted line indicate the position $x = 32.9$ nm. (b) Same as (a), but for $r_{cut} = 3.4$ nm. (c) Same as (a) and (b), but for $r_{cut} = 5.5$ nm.

valence band (VBM-1) has a hybrid character, slightly shifted towards MoSe$_2$, making the wave functions corresponding to this band delocalized over both layers. At the Γ point, the highest valence band also has a strong hybrid character. The indirect band gap between K and Γ measures $E_{K\Gamma} = 1.13$ eV,
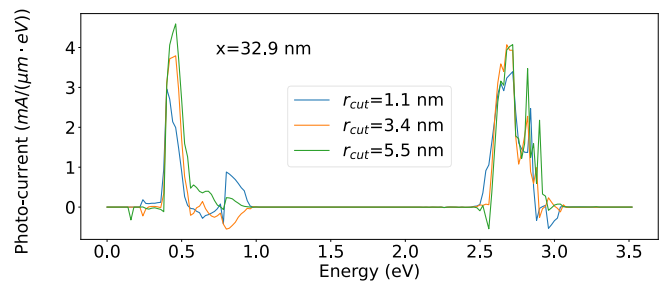

FIG. 5. Energy-resolved photocurrent at position $x = 32.9$ nm in Fig. 4 for the three different cutoff radii $r_{cut} = 1.1$, 3.4, and 5.5 nm considered here.

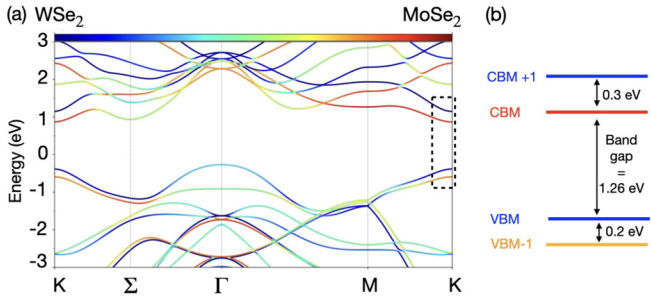FIG. 6. (a) Partial band structure of the considered MoSe$_2$-WSe$_2$ van der Waals heterostructure projected onto the orbitals of MoSe$_2$ (red) and WSe$_2$ (blue). (b) Zoom into the dashed black box in (a). The energy levels belonging to the different TMDs at the K point are shown.

while the direct one at K is equal to 1.26 eV. The distance at K between CBM and CBM + 1 is 0.3 eV, the distance between VBM and VBM-1 0.2 eV [see Fig. 6(b)]. Our findings are consistent with other theoretical studies [34,46].

Figure 7 shows the interband light-matter coupling matrix elements $M_{\alpha\beta}^x(\vec{k})$ for the MoSe$_2$-WSe$_2$ vdWH evaluated between different conduction and valence bands on a uniform k-point mesh in the entire Brillouin zone using a light polarization aligned with the in-plane x axis ($\vec{e}_x$). The $M_{\alpha\beta}^x(\vec{k})$ is obtained from the $M_{nm}^x(\vec{k})$ in the localized orbital basis of Eq. (9) as

$$M_{\alpha\beta}^x(\vec{k}) = \sum_{nm} c_\alpha^{n*}(\vec{k}) M_{nm}^x(\vec{k}) c_\beta^m(\vec{k}), \qquad (11)$$

where $c_\alpha^n(\vec{k})$ and $c_\beta^m(\vec{k})$ are the coefficients of the wave function in the MLWF basis. They correspond to the nth and mth entries of the eigenstates of the MLWF Hamiltonian at $\vec{k}$, for the bands α and β, respectively. It can be first observed that the $M_{\alpha\beta}^x(\vec{k})$'s strongly vary with respect to the momentum vector. For instance, the value at K in subplot (a) is much smaller than the one at Σ for the coupling between CBM and VBM. This can be explained by the fact that, at K, the two considered bands belong to different TMDs, i.e., their wave functions barely overlap, while at Σ, the lower valence band belongs to MoSe$_2$, while the conduction band has a hybrid character, i.e., its wave function is delocalized over both TMDs. The same happens at Γ, but the resulting momentum operator is almost negligible there, although this transition is not forbidden by the symmetry of the wave function. Note also that the band gaps at Σ (2 eV) and at Γ (2 eV) are much larger than at K (1.26 eV) so that no transition is expected to occur at these points.

Figures 7(b) and 7(c) depict the same quantity as in Fig. 7(a), but evaluated between CBM + 1 and VBM and between CBM and VBM-1, respectively. In these cases, $M_{\alpha\beta}^x(K)$ connects bands that belong to the same TMDs (intralayer) or have a hybrid character. The reported values are therefore much larger than when the bands are situated in different TMDs (interlayer), as in Fig. 7(a). At first sight, it appears highly unlikely that interlayer electron-hole pairs can be directly created through light absorption at the K point. They should be first generated inside the same monolayer and then one charge carrier should be transferred to the other layer via, for example, phonon emission processes [34]. In the following, we will demonstrate that despite the weak interlayer matrix element, it is still possible to generate interlayer
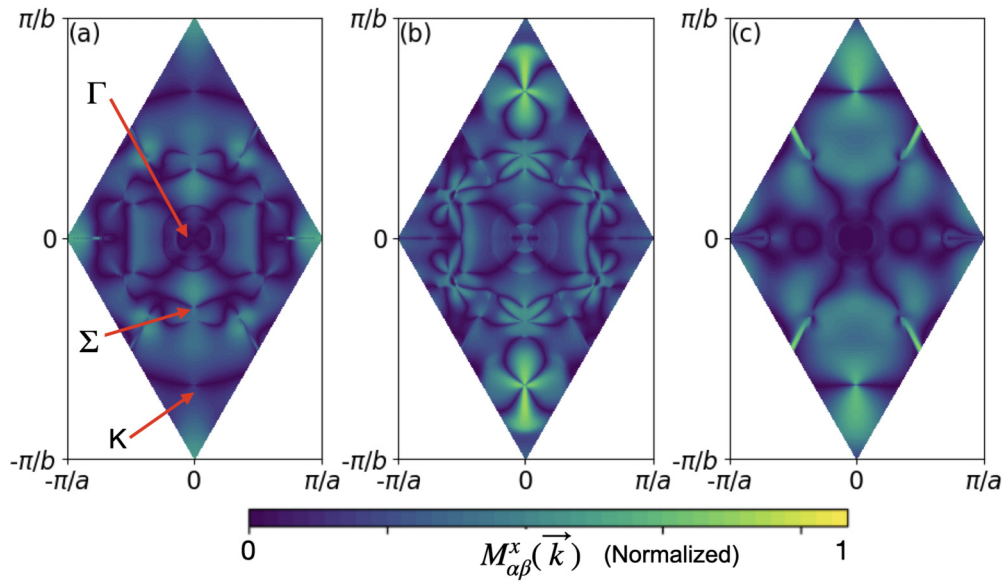

FIG. 7. (a) Light-matter coupling matrix element $M_{\alpha\beta}^x(\vec{k})$ from Eq. (11) for a light polarization aligned with the in-plane x axis evaluated between the lowest conduction band (CBM) and the highest valence band (VBM) of the MoSe$_2$-WSe$_2$ heterostructure in the entire Brillouin Zone. Green/yellow (blue/black) indicates a high (low) value of $M_{\alpha\beta}^x(\vec{k})$. The high symmetry points, K, Γ, and Σ are explicitly marked. (b) Same as (a), but for $M_{\alpha\beta}^x(\vec{k})$ evaluated between the second lowest conduction band (CBM + 1) and the highest valence band (VBM) of the MoSe$_2$-WSe$_2$ heterostructure. (c) Same as (a), but for $M_{\alpha\beta}^x(\vec{k})$ evaluated between the lowest conduction band (CBM) and the second highest valence band (VBM-1) of the MoSe$_2$-WSe$_2$ vdWH.
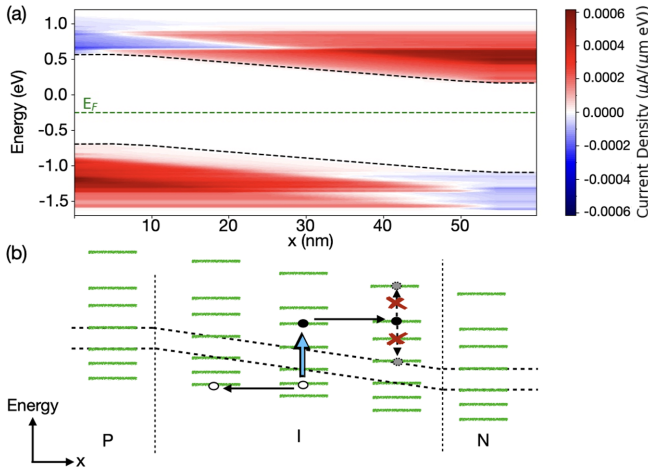
FIG. 8. (a) Spectral and spatial distribution of the photocurrent flowing through a $MoSe_2$-WSe_2 PIN photodiode at $k_z = K$ using a photon energy $E_{ph} = 1.8$ eV and a built-in potential of 0.4 eV. The Fermi level is indicated by the dashed green line. The conduction ($MoSe_2$) and valence (WSe_2) band edges are represented by the dashed black lines. Red indicates electrons (holes) moving towards the N(P) side, which is situated on the right (left) of the device. Blue refers to the opposite direction. (b) Sketch of the elastic processes occurring in (a). The solid green lines represent energy levels. Empty and filled circles are holes and electrons, respectively. The blue arrow shows the creation of an electron-hole pair, which is then coherently separated by the electric field. Relaxation (promotion) into lower (higher) energy states is not accounted for in our model.

electron-hole pairs in a coherent way, without phonon assistance, by leveraging the hybrid character of the second highest valence band, which is delocalized over the $MoSe_2$ and WSe_2 monolayers.

B. Photocurrent analysis

The spatial and spectral resolution of the photocurrent in the $MoSe_2$-WSe_2 vdW PIN photodiode is given in Fig. 8(a) using $E_{ph} = 1.8$ eV and a built-in potential of 0.4 V. Once an electron-hole pair is created through light absorption, electrons in the conduction band and holes in the valence band are accelerated by the electric-field of the intrinsic region towards the contacts of the PIN junction. However, since no inelastic processes are considered [Fig. 8(b)], states have to be available at the same energy throughout the device to allow for electrons (holes) to flow toward the N (P) side and be collected there. When this condition is satisfied, a positive current is observed. It is represented by the red background in Fig. 8(a). The blue background, instead, depicts the condition for which electrons are driven towards the P side and holes towards the N side. Due to the weak electric field in the regions near contacts, most photoexcited electron-hole pairs are not separated before being collected. This leads to the negative current densities seen in Fig. 8.

To continue our analysis, we investigated the electron (I^e) and hole (I^h) components of the photocurrent. For that purpose, we set the built-in potential to 0.2 V and the photon energy to 1.8 eV. We chose a built-in potential lower than the energy difference between CBM and CBM + 1 as well
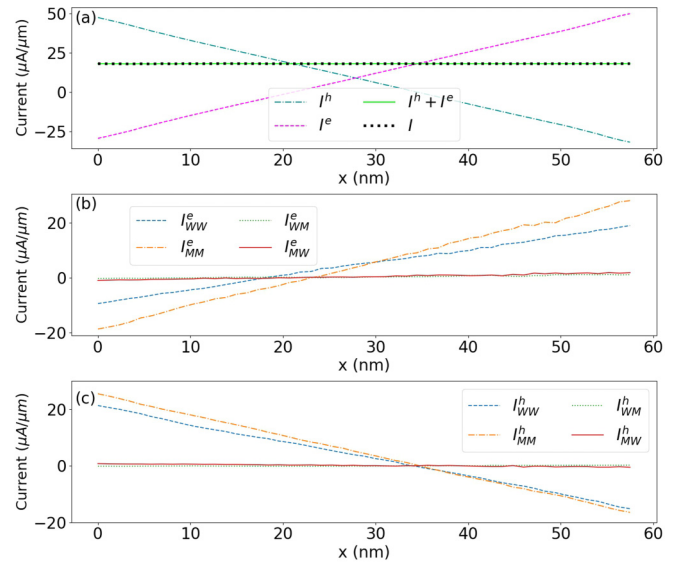

FIG. 9. (a) Photocurrent flowing through a $MoSe_2$-WSe_2 PIN photodiode with a built-in potential of 0.2 V and a photon energy $E_{ph} = 1.8$ eV. The variable I^e (I^h) refers to the electron (hole) current, while $I = I^e + I^h$ is the total current as obtained from a full-band simulation (black dots) or after separating the electron and hole contributions (green line). (b) Decomposition of the electron photocurrent in (a). I^e_{MM} (I^e_{WW}) is the electron current flowing between atoms in the $MoSe_2$ (WSe_2) layer, while I^e_{MW} (I^e_{WM}) is the current flowing from atoms in the $MoSe_2$ (WSe_2) layer to atoms in the WSe_2 ($MoSe_2$) layer. (c) Same of (b), but for holes.

as between VBM and VBM-1 in Fig. 6(b) in order to suppress any interlayer tunneling path and to simplify the following analysis of our results. First, we performed a simulation over the entire electron and hole energy spectrum of interest, i.e., the energy range goes from below the valence band edge of $MoSe_2$ to above the conduction band edge of WSe_2. After running this simulation, all self-energy matrices were stored. We then decomposed the current into I^e and I^h by passing the self-energies corresponding to the appropriate energies as inputs to two new simulations. The calculation of the hole photocurrent relies on energies below the Fermi level in Fig. 8, while its electron counterpart is obtained by summing up the contributions above the Fermi level. As shown in Fig. 9(a), adding up the electron and hole components produces the same current as obtained with the full energy spectrum. This demonstrates that the separation of the scattering self-energies still delivers the expected result. Moreover, the hole current dominates on the P side of the diode, the electron current on the N side, while they have the same value almost in the middle of the intrinsic region.

Going one step further, an atomistic resolution of the photocurrent can be realized by applying Eq. (10) between different atoms instead of different cells. We therefore divided the current into intralayer [electrons and holes flow between atoms in WSe_2 (I_{WW}) or $MoSe_2$ (I_{MM})] and interlayer [carriers are either transferred from WSe_2 to $MoSe_2$ (I_{WM}) or from $MoSe_2$ to WSe_2 (I_{MW})] contributions. The inter and intralayer photocurrents for electron and holes are presented in Figs. 9(b) and 9(c), respectively. It can be observed that
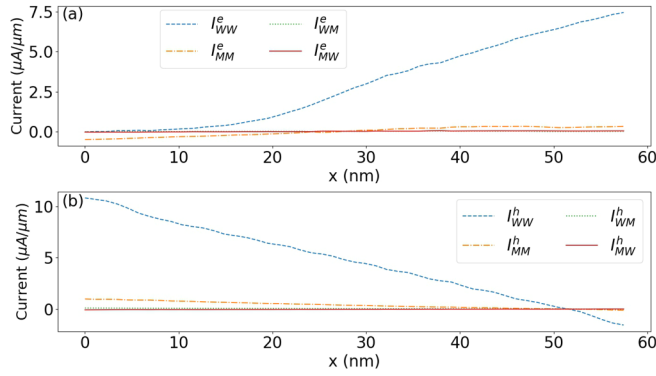
FIG. 10. (a) Electron photocurrent flowing through the MoSe$_2$-WSe$_2$ PIN photodiode in Fig. 1 with a built-in potential of 0.2 V and a photon energy equal to 1.55 eV. Only the contributions to the momentum operator between atoms situated in WSe$_2$ are considered (P-WW). The I^e_{MM}, I^e_{WW}, I^e_{MW}, and I^e_{WM} quantities have the same meaning as in Fig. 9. (b) Same of (a), but for holes.
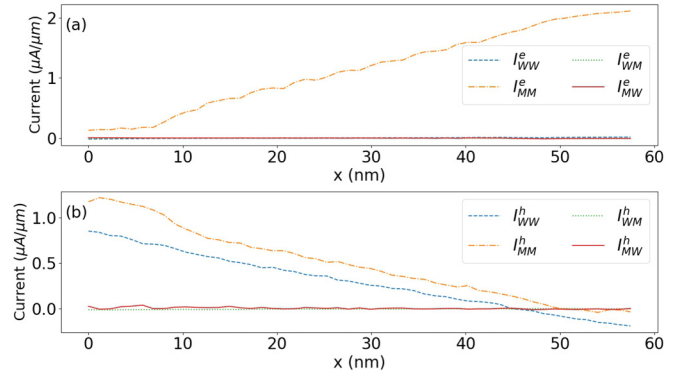
FIG. 11. Same as Fig. 10, but with a photon energy equal to 1.46 eV and considering only the contributions to the momentum operator between atoms located in MoSe$_2$ (P-MM).

I_{WW} and I_{MM} exhibit similar behaviours for both electrons and holes, increasing (decreasing) from the left to the right for electrons (holes). This indicates that carriers are generated with almost the same probability in both monolayers. As I_{MW} and I_{WM} are extremely small it can be deduced that the electrons and holes remain in the monolayer where they were created: there is almost no charge transfer from one layer to the other.

Based on these results, it is not possible to determine whether electron-hole pairs are generated across the MoSe$_2$ and WSe$_2$ monolayers (interlayer) or only inside the individual TMDs (intralayer). To address this question, the PIN built-in potential was kept at 0.2 eV and only the momentum operator entries in Eq. (9) connecting atoms within the WSe$_2$ monolayer (P-WW) were retained, as if we were only shining light onto that material. A photon energy of 1.55 eV was selected, in order to connect VBM and CBM + 1 at the K point (Fig. 6). Figure 10 shows that both the electron and hole currents reside inside the WSe$_2$ layer: almost no interlayer electron-hole pairs are created as the I_{MW} and I_{WM} contributions can be barely detected and thus only a very small I_{MM} is present.

Finally, the same experiment was repeated, but keeping only the momentum operator entries connecting atoms within the MoSe$_2$ monolayer, i.e., P-MM. The photon energy was set to 1.46 eV, in order to connect VBM-1 and CBM. As expected, all electrons are created within MoSe$_2$ (I^e_{MM}) and they remain there, as can be seen in Fig. 11(a), because the built-in potential (0.2 eV) is smaller than the energy difference between CBM and CBM + 1 (0.3 eV). Hence, electrons cannot gain enough excess energy to overcome the energy difference and tunnel from the MoSe$_2$ to the WSe$_2$ layer.

Holes, instead, are generated both in MoSe$_2$ and WSe$_2$ [Fig. 11(b)] since the VBM-1 wave function is delocalized over both monolayers (Fig. 6). As a consequence, the behavior of I^h_{WW} is very similar to that of I^h_{MM}. The electron-hole pairs created in this case either belong to the same layer (MoSe$_2$) or are generated across both layers (electrons in MoSe$_2$ and holes in WSe$_2$). These interlayer electron-hole pairs are physically separated in space and less susceptible to recombine than those localized in the same monolayer. To obtain an interlayer exciton between CBM and VBM and not between CBM and VBM-1, the holes situated in WSe$_2$ should release their extra kinetic energy by emitting phonons and relax from VBM-1 to VBM. Once this is done, they can interact and bind with an electron in MoSe$_2$. As compared to the widely assumed theory of interlayer excitons formation via charge transfer, no phonon-assisted tunneling is directly required in the mechanism proposed here, as shown by the small interlayer currents I_{MW} and I_{WM} in Fig. 11. It should nevertheless be emphasized that the photoexcited currents in Fig. 11 (MoSe$_2$ illumination) are 3 to 5 times lower than in Fig. 10 (WSe$_2$ illumination). The interlayer processes, although efficient, are less strong than the intralayer ones.

We would like to point out that the localized and delocalized nature of the wave functions strongly depends on the stacking order. The electronic dispersion projected onto the orbitals of the selected MoSe$_2$-WSe$_2$ system is given in Fig. 12 for two different stacking orders. Subplot (a) shows the result obtained for the AA' stacking, the one used in this paper, while subplot (b) presents the band structure of the AA stacking where the transition metal (chalcogenide) atoms of the top layer are aligned with the transition metal (chalcogenide) of the bottom layer. At the K point the second highest valence band, highlighted by a dotted circle, is localized in the MoSe$_2$ monolayer in the AA stacking, contrary to the case with AA' stacking, where it is delocalized. If the same numerical experiment as in Fig. 11 is repeated for the AA stacking (only contribution to the momentum operator for atoms in MoSe$_2$), all electron-hole pairs are generated in MoSe$_2$, as can be seen in Fig. 13. It is therefore clear that the interlayer electron-hole pairs originate from the delocalized VBM-1 band in the AA' stacking case.

C. Influence of spin-orbit coupling (SOC)

Since SOC is crucial to understand TMDC systems [74], we performed additional calculations including this effect and compared them to results without it. For our MoSe$_2$-WSe$_2$ vdWH with the AA' stacking, including the SOC leads to a
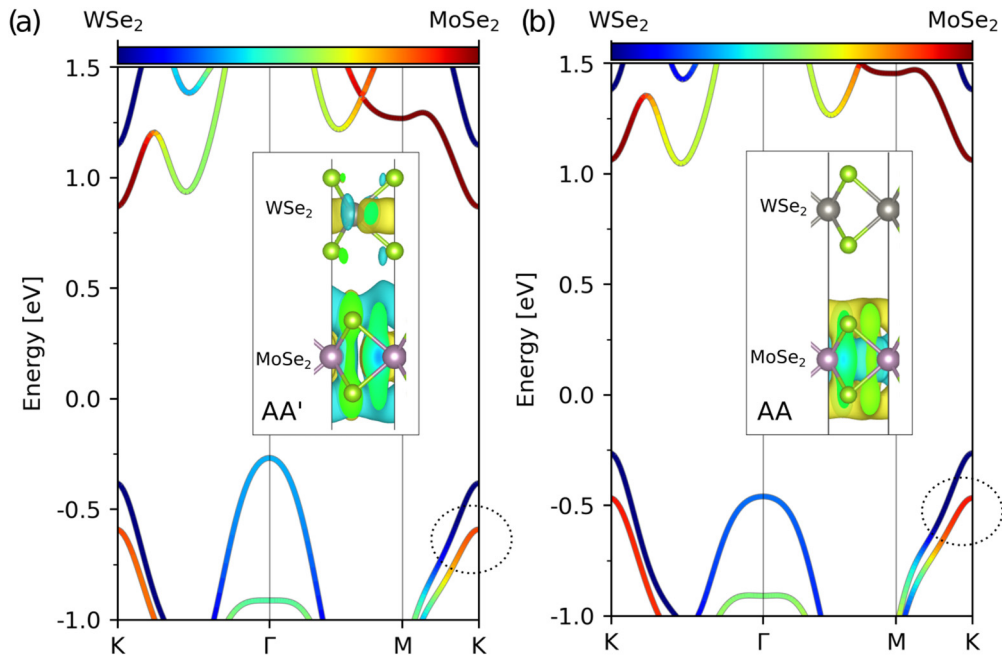
FIG. 12. (a) Partial band structure of a AA'-stacked $MoSe_2$-WSe_2 vdWH projected onto the orbitals of $MoSe_2$ (red) and WSe_2 (blue). (b) Same as (a), but for the AA stacking. The inset in each subfigure shows the Kohn-Sham wave functions of the second highest valence band (VBM-1) at K that is circulated.

reduced direct band gap at the K point, as shown in Fig. 14. SOC has a particularly strong influence on the VBs, where the two upper bands split into four bands. The lowest CB is less affected by SOC, while the second lowest CB undergoes a stronger variation. Particularly, the direct band gap at the K point is reduced from 1.26 to 1.01 eV by SOC. Importantly, the second and third VB wave functions at the K point in the calculation with SOC exhibit a similar delocalization character as the (VBM-1) wave function in the calculation without SOC, as depicted in Fig. 14. The magnitude of the wave function appears smaller with SOC due to the usage of a different normalization in both cases.

Next, we recalculated the photocurrent flowing through the considered vdWH in the presence of SOC. As an example, we used $E_{ph} = 2.1$ eV and a built-in potential energy of 0.4 eV. The photocurrent is reduced after including SOC by a relative variation of around 20%. In view of the strong effect of SOC

on the band structure, such variation is expected. Hence, even though including SOC quantitatively affects the value of the photocurrent, it does not alter the main conclusion of our work, namely that interlayer excitons can be created without the need for electron-phonon interactions.

D. Impact of the interlayer distance

DFT typically struggles at determining the exact equilibrium distance between adjacent layers in van der Waals heterostructures due to the long-range correlation effects of van der Waals interactions. It is therefore of practical interest to examine the influence of the interlayer distance on the band structure and photocurrent of our $MoSe_2$-WSe_2 device. We artificially changed the interlayer distance from +3% to −1% with respect to the equilibrium distance of the fully relaxed structure. Figure 15 shows that the band structure is very weakly affected by the interlayer distance and the largest variation happens at the Γ point, not at the K point where most of the light is absorbed.

The wave function delocalization between the layers is compared for all these cases. We notice that the delocalization is slightly sensitive to the interlayer distance, remaining similar, from the +3% to the −1% case. The shorter the interlayer distance, the stronger the wave function delocalization appears. Next, we computed the photocurrent based on these DFT results relying on different interlayer distances. Here again, we used $E_{ph} = 2.1$ eV and a built-in potential energy of 0.4 eV. No noticeable variation of the photocurrent is observed when the interlayer goes from −1% (39.8 $\mu A/\mu m$) to +3% (39.7 $\mu A/\mu m$). It can thus be concluded that the uncertainty in the interlayer distance does not qualitatively change the findings of our paper.
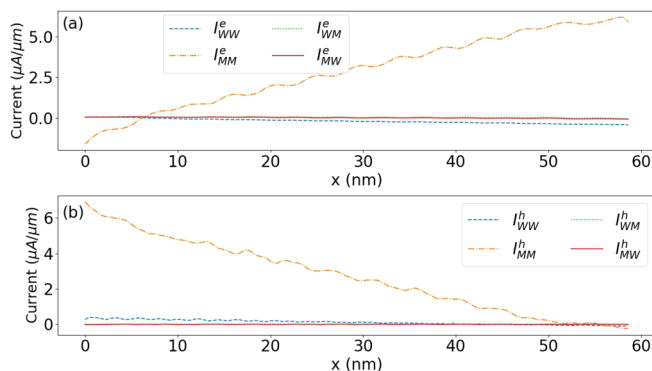

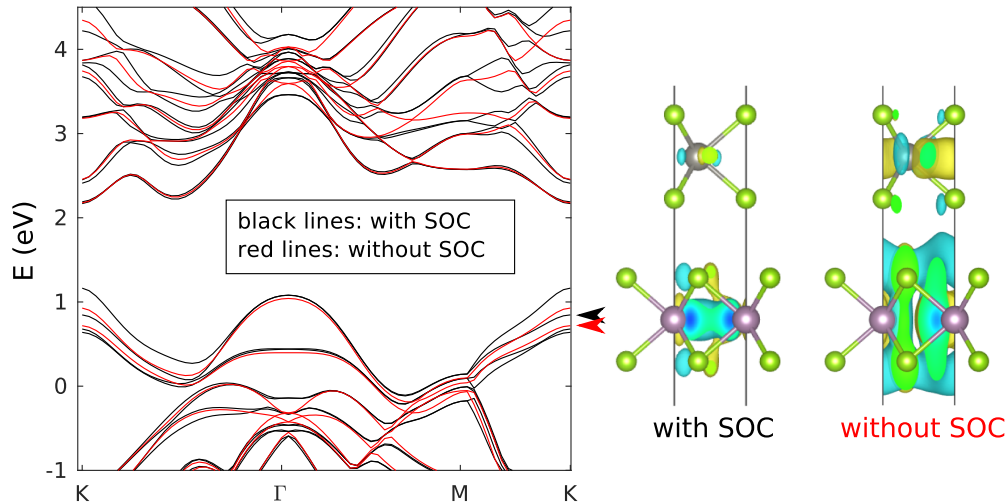FIG. 13. Same as Fig. 11, but for the AA stacking order of the $MoSe_2$-WSe_2 vdWH.

FIG. 14. Band structure of the MoSe$_2$-WSe$_2$ with and without SOC. The arrow indicates the second highest valence band at the K point. The plots on the right side show the corresponding wave function.

E. Excitonic effects

Excitonic effects profoundly affect the photoconductivity and other optoelectronic properties of layered TMDCs and their vdWHs due to their combination of a 2D planar structure and strong Coulomb interactions. On the one hand, large excitonic binding energies enhance the optical absorption of TMDCs, which could potentially lead to higher photocon-

FIG. 15. (a) Band structure of the MoSe$_2$-WSe$_2$ heterostructure with interlayer distance varied from $+3\%$ to -1% as compared to equilibrium distance obtained using PBE. (b) Wave function of the second highest valence band at the K point for different interlayer distances.

ductivity. On the other hand, larger exciton binding energy requires stronger electric fields to ionize the excitons into charged carriers and generate a photocurrent. Previous theoretical investigations of monolayer MoS$_2$ predicted that the ionization time of exciton in this material decays exponentially when increasing the in-plane electric field [75]. For an electric field strength similar to the one used in our simulations (about 0.01 V/nm), the ionization time is expected to be below 0.1 ns for monolayer MoS$_2$. We expect similar values and orders of magnitude for the ionization time of monolayer MoSe$_2$ and WSe$_2$.

As photocurrent generation has been experimentally observed in MoSe$_2$-WSe$_2$ vdWHs by several groups working with similar structures as the one studied here, it can be deduced that the possibility of dissociating interlayer excitons exists in the devices modeled in this paper. Due to the type-II band alignment and the atomically sharp interface in the van der Waals heterostructures, the interlayer vertical electric field is strong, which results in the ultrafast charge transfer between the two layers [8,76]. Interlayer excitons with a reduced binding energy and much longer lifetime facilitate the ionization by in-plane electric field. However, considering that the effect of exciton ionization could still overwhelm the increase of absorption, our results should probably be seen as some kind of upper limit for the photocurrents flowing through MoSe$_2$-WSe$_2$ vdWHs. To definitively assess the impact of excitons on the creation of interlayer excitons and their dissociation into moving electron-hole pairs, a more sophisticated simulation approach is needed that goes beyond the scope of this paper.

V. CONCLUSIONS

We developed a theoretical framework to compute the photogeneration of electron-hole pairs and carrier transport in van der Waals heterostructures at the quantum mechanical level using many-body perturbation theory and the nonequilibrium Green's function formalism. The electronic Hamiltonian and electron-photon coupling matrix elements are obtained from density functional theory calculations, thus avoiding the need
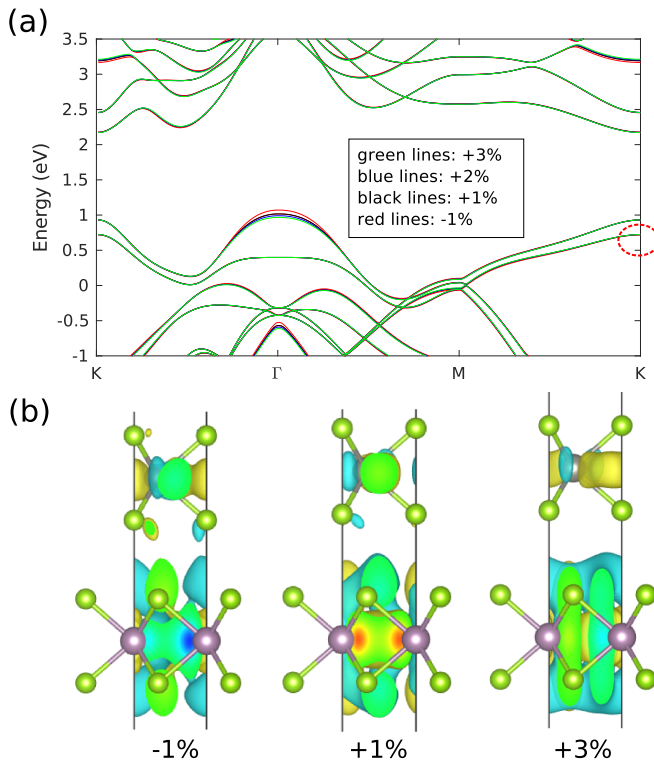
for fitting parameters. Utilizing this simulation environment, we investigated light-matter interactions in MoSe$_2$-WSe$_2$-based PIN photodiodes illuminated by a monochromatic light, polarized along the x axis, and vertically incident on the device. We found that the localized nature of the wave functions, which can be controlled by the stacking order, allows to generate and maintain an electron or hole photocurrent exclusively in one of the monolayers. When, instead, a band is delocalized, both intra- and interlayer electron-hole pairs can be generated, paving the way for the formation of interlayer excitons.

In reality, the exchange of momentum between phonons and electrons may play an additional important role in processes involving light-matter interactions. For instance, they may enable electrons and holes to move from the K to the Γ or Σ valley in the Brillouin zone where the interlayer coupling is stronger than at K. Electron-phonon scattering can be readily included in the framework developed in this work. However, despite using efficient parallel numerical algorithms, the inclusion of both electron-photon and electron-phonon interactions at the *ab initio* level requires prohibitively high computational resources and could not be applied here. The usage of a phenomenological electron-phonon scattering model could be a solution to this problem and will be tested in the future.

ACKNOWLEDGMENTS

APPENDIX: CONSTRUCTION OF THE HAMILTONIAN MATRIX

Periodic boundary conditions along z are imposed to the Hamiltonian matrix by introducing a k_z-dependence according to

$$H(k_z) = \sum_{n \in \{-\infty, \dots, -1, 0, 1, \infty\}} H_{(n)} e^{ink_z \Delta_z}. \quad (A1)$$

Here, $H_{(n)}$ describes the hoping Hamiltonian matrix connecting the central orthorhombic transport cell to its periodic replica situated at $z = z_0 + n\Delta_z$, where Δ_z is the width of the central cell along z and z_0 its position while $-\pi/\Delta_z \leqslant k_z < \pi/\Delta_z$. Typically, the transport unit cell is made large enough so that only coupling to nearest-neighbor cells exists, i.e., $n \in \{-1, 0, 1\}$. Going beyond nearest-neighbor cell coupling by decreasing the transport cell (here up to second nearest-neighbor, $n \in \{-2, -1, 0, 1, 2\}$) allows to reduce the computational burden. It should however be noted that reducing the size of the considered unit cell should be compensated by a proportional increase of the number of k_z momentum points (Nk_z) along the z direction, to keep the same accuracy. Since the computational complexity for the calculation of the Green's function is proportional to $Nk_z \times N_{O,UC}^3$, $N_{O,UC}$ being the number of orbitals in the transport cell, scaling $N_{O,UC}$ by a factor α and multiplying Nk_z by the same factor is advantageous, with a potential gain of α^2. When different k_z's are coupled to each other through scattering self-energies, as encountered for example with electron-phonon interactions, a higher number of k_z's is undesirable because the computational intensity grows quadratically with Nk_z, i.e., it is proportional to $N_{k_z}^2 \times N_A$. As typically the time to compute k_z-dependent scattering self-energies dominates over that required to solve the Green's functions. The benefit of reducing the size of the transport unit cell vanishes in most cases. With electron-photon interactions, the situation is different as all k_z's are independent of each other due to the negligible magnitude of the photon momentum as compared to the electron one. Applying the trick in Eq. (A1) then becomes computationally attractive.

[1] M.-H. Chiu, M.-Y. Li, W. Zhang, W.-T. Hsu, W.-H. Chang, M. Terrones, H. Terrones, and L.-J. Li, ACS Nano **8**, 9649 (2014).

[2] P. Rivera, J. R. Schaibley, A. M. Jones, J. S. Ross, S. Wu, G. Aivazian, P. Klement, K. Seyler, G. Clark, N. J. Ghimire, J. Yan, D. G. Mandrus, W. Yao, and X. Xu, Nat. Commun. **6**, 6242 (2015).

[3] Y. Jiang, S. Chen, W. Zheng, B. Zheng, and A. Pan, Light Sci. Appl. **10**, 72 (2021).

[4] P. Nagler, G. Plechinger, M. V. Ballottin, A. Mitioglu, S. Meier, N. Paradiso, C. Strunk, A. Chernikov, P. C. Christianen, C. Schüller *et al.*, 2D Mater. **4**, 025112 (2017).

[5] L. A. Jauregui, A. Y. Joe, K. Pistunova, D. S. Wild, A. A. High, Y. Zhou, G. Scuri, K. De Greve, A. Sushko, C.-H. Yu *et al.*, Science **366**, 870 (2019).

[6] M. Palummo, M. Bernardi, and J. C. Grossman, Nano Lett. **15**, 2794 (2015).

[7] S. Ovesen, S. Brem, C. Linderälv, M. Kuisma, T. Korn, P. Erhart, M. Selig, and E. Malic, Commun. Phys. **2**, 23 (2019).

[8] P. Rivera, K. L. Seyler, H. Yu, J. R. Schaibley, J. Yan, D. G. Mandrus, W. Yao, and X. Xu, Science **351**, 688 (2016).

[9] J. Kiemle, F. Sigger, M. Lorke, B. Miller, K. Watanabe, T. Taniguchi, A. Holleitner, and U. Wurstbauer, Phys. Rev. B **101**, 121404(R) (2020).

[10] H. Zhou, Y. Zhao, W. Tao, Y. Li, Q. Zhou, and H. Zhu, ACS Nano **14**, 4618 (2020).

[11] K.-Q. Lin, Light Sci. Appl. **10**, 99 (2021).

[12] C. Choi, J. Huang, H.-C. Cheng, H. Kim, A. K. Vinod, S.-H. Bae, V. O. Özçelik, R. Grassi, J. Chae, S.-W. Huang, X. Duan, K. Kaasbjerg, T. Low, and C. W. Wong, npj 2D Mater. Appl. **2**, 30 (2018).

[13] H. C. Kamban and T. G. Pedersen, Sci. Rep. **10**, 5537 (2020).

[14] L. Zhang, R. Gogna, G. W. Burg, J. Horng, E. Paik, Y.-H. Chou, K. Kim, E. Tutuc, and H. Deng, Phys. Rev. B **100**, 041402(R) (2019).

[15] M. M. Furchi, A. Pospischil, F. Libisch, J. Burgdörfer, and T. Mueller, Nano Lett. **14**, 4785 (2014).

[16] N. Flöry, A. Jain, P. Bharadwaj, M. Parzefall, T. Taniguchi, K. Watanabe, and L. Novotny, Appl. Phys. Lett. **107**, 123106 (2015).

[17] W. Choi, I. Akhtar, D. Kang, Y.-j. Lee, J. Jung, Y. H. Kim, C.-H. Lee, D. J. Hwang, and Y. Seo, Nano Lett. **20**, 1934 (2020).

[18] M. Combescot, R. Combescot, and F. Dubin, Rep. Prog. Phys. **80**, 066501 (2017).

[19] A. A. High, E. E. Novitskaya, L. V. Butov, M. Hanson, and A. C. Gossard, Science **321**, 229 (2008).

[20] L. V. Butov, J. Phys.: Condens. Matter **19**, 295202 (2007).

[21] S. Charbonneau, M. L. W. Thewalt, E. S. Koteles, and B. Elman, Phys. Rev. B **38**, 6287 (1988).

[22] M. V. Stern, Y. Waschitz, W. Cao, I. Nevo, K. Watanabe, T. Taniguchi, E. Sela, M. Urbakh, O. Hod, and M. B. Shalom, Science **372**, 1462 (2021).

[23] L. Yuan, B. Zheng, J. Kunstmann, T. Brumme, A. B. Kuc, C. Ma, S. Deng, D. Blach, A. Pan, and L. Huang, Nat. Mater. **19**, 617 (2020).

[24] P. Rivera, H. Yu, K. L. Seyler, N. P. Wilson, W. Yao, and X. Xu, Nat. Nanotechnol. **13**, 1004 (2018).

[25] M. Baranowski, A. Surrente, L. Klopotowski, J. M. Urban, N. Zhang, D. K. Maude, K. Wiwatowski, S. Mackowski, Y. C. Kung, D. Dumcenco, A. Kis, and P. Plochocka, Nano Lett. **17**, 6360 (2017).

[26] M. M. Ugeda, A. J. Bradley, S.-F. Shi, H. Felipe, Y. Zhang, D. Y. Qiu, W. Ruan, S.-K. Mo, Z. Hussain, Z.-X. Shen *et al.*, Nat. Mater. **13**, 1091 (2014).

[27] A. M. Jones, H. Yu, N. J. Ghimire, S. Wu, G. Aivazian, J. S. Ross, B. Zhao, J. Yan, D. G. Mandrus, D. Xiao *et al.*, Nat. Nanotechnol. **8**, 634 (2013).

[28] A. Ramasubramaniam, Phys. Rev. B **86**, 115409 (2012).

[29] T. Cheiwchanchamnangij and W. R. L. Lambrecht, Phys. Rev. B **85**, 205302 (2012).

[30] C.-H. Lee, G.-H. Lee, A. M. Van Der Zande, W. Chen, Y. Li, M. Han, X. Cui, G. Arefe, C. Nuckolls, T. F. Heinz *et al.*, Nat. Nanotechnol. **9**, 676 (2014).

[31] F. Ceballos, M. Z. Bellus, H.-Y. Chiu, and H. Zhao, ACS Nano **8**, 12717 (2014).

[32] X. Zhu, N. R. Monahan, Z. Gong, H. Zhu, K. W. Williams, and C. A. Nelson, J. Am. Chem. Soc. **137**, 8313 (2015).

[33] X. Hong, J. Kim, S.-F. Shi, Y. Zhang, C. Jin, Y. Sun, S. Tongay, J. Wu, Y. Zhang, and F. Wang, Nat. Nanotechnol. **9**, 682 (2014).

[34] Q. Zheng, W. A. Saidi, Y. Xie, Z. Lan, O. V. Prezhdo, H. Petek, and J. Zhao, Nano Lett. **17**, 6435 (2017).

[35] S. Rajabali, E. Cortese, M. Beck, S. De Liberato, J. Faist, and G. Scalari, Nat. Photonics **15**, 690 (2021).

[36] J. Chen, Y. Hu, and H. Guo, Phys. Rev. B **85**, 155441 (2012).

[37] E. Lopriore, E. G. Marin, and G. Fiori, Nanoscale Horiz. **7**, 41 (2021).

[38] S. Aas and C. Bulutay, Opt. Express **26**, 28672 (2018).

[39] D. A. Stewart and F. Léonard, Phys. Rev. Lett. **93**, 107401 (2004).

[40] D. A. Stewart and F. Léonard, Nano Lett. **5**, 219 (2005).

[41] U. Aeberhard, J. Comput. Electron. **10**, 394 (2011).

[42] U. Aeberhard, J. Phys. D: Appl. Phys. **51**, 323002 (2018).

[43] M. F. Pereira and K. Henneberger, Phys. Rev. B **58**, 2064 (1998).

[44] L. E. Henrickson, J. Appl. Phys. **91**, 6273 (2002).

[45] Y. Hirokawa, A. Yamada, S. Yamada, M. Noda, M. Uemoto, T. Boku, and K. Yabana, Int. J. High Perform. Comput. Appl. **36**, 182 (2022).

[46] H.-P. Komsa and A. V. Krasheninnikov, Phys. Rev. B **88**, 085318 (2013).

[47] M. Bernardi, M. Palummo, and J. C. Grossman, Nano Lett. **13**, 3664 (2013).

[48] B. Amin, N. Singh, and U. Schwingenschlögl, Phys. Rev. B **92**, 075439 (2015).

[49] L. V. Keldysh, Sov. Phys. JETP **20**, 1018 (1965).

[50] A. L. Fetter and J. D. Walecka, *Quantum Theory of Many-Particle Systems* (Dover Publications, New York, 2012).

[51] S. Datta, in *Digest. International Electron Devices Meeting* (IEEE, San Francisco, CA, 2002), pp. 703–706.

[52] A. A. Mostofi, J. R. Yates, Y.-S. Lee, I. Souza, D. Vanderbilt, and N. Marzari, Comput. Phys. Commun. **178**, 685 (2008).

[53] A. N. Ziogas, T. Ben-Nun, G. I. Fernández, T. Schneider, M. Luisier, and T. Hoefler, in *Proceedings of the International Conference for High Performance Computing, Networking, Storage and Analysis, SC '19* (Association for Computing Machinery, New York, 2019).

[54] Szabó, S. J. Koester, and M. Luisier, IEEE Electron Device Lett. **36**, 514 (2015).

[55] M. Luisier and G. Klimeck, Phys. Rev. B **80**, 155430 (2009).

[56] S. Brück, M. Calderara, M. H. Bani-Hashemian, J. VandeVondele, and M. Luisier, J. Chem. Phys. **147**, 074116 (2017).

[57] A. Kuzmin, M. Luisier, and O. Schenk, in *Euro-Par 2013 Parallel Processing*, edited by F. Wolf, B. Mohr, and D. an Mey (Springer, Berlin, Heidelberg, 2013), pp. 533–544.

[58] M. Bollhöfer, A. Eftekhari, S. Scheidegger, and O. Schenk, SIAM J. Sci. Comput. **41**, A380 (2019).

[59] M. P. Anantram, M. S. Lundstrom, and D. E. Nikonov, Proc. IEEE **96**, 1511 (2008).

[60] C. Klinkert, Ph.D. thesis, ETH Zurich, 2021.

[61] N. Cavassilas, F. Michelini, and M. Bescond, J. Comput. Electron. **15**, 1233 (2016).

[62] R. Lake, G. Klimeck, R. C. Bowen, and D. Jovanovic, J. Appl. Phys. **81**, 7845 (1997).

[63] J. He, K. Hummer, and C. Franchini, Phys. Rev. B **89**, 075409 (2014).

[64] J. Shi, R. Tong, X. Zhou, Y. Gong, Z. Zhang, Q. Ji, Y. Zhang, Q. Fang, L. Gu, X. Wang *et al.*, Adv. Mater. **28**, 10664 (2016).

[65] J.-J. Ma, J.-J. Zheng, X.-L. Zhu, P.-F. Liu, W.-D. Li, and B.-T. Wang, Phys. Chem. Chem. Phys. **21**, 10442 (2019).

[66] G. Kresse and J. Furthmüller, Phys. Rev. B **54**, 11169 (1996).

[67] G. Kresse and J. Furthmüller, Comput. Mater. Sci. **6**, 15 (1996).

[68] J. P. Perdew, K. Burke, and M. Ernzerhof, Phys. Rev. Lett. **77**, 3865 (1996).

[69] S. Grimme, J. Comput. Chem. **27**, 1787 (2006).

[70] L. Yu, V. Ranjan, W. Lu, J. Bernholc, and M. Buongiorno Nardelli, Phys. Rev. B **77**, 245102 (2008).

[71] Á. Szabó, R. Rhyner, and M. Luisier, Phys. Rev. B **92**, 035435 (2015).

[72] E. Najafidehaghani, Z. Gan, A. George, T. Lehnert, G. Q. Ngo, C. Neumann, T. Bucher, I. Staude, D. Kaiser, T. Vogl, U. Hübner, U. Kaiser, F. Eilenberger, and A. Turchanin, Adv. Funct. Mater. **31**, 2101086 (2021).

[73] X. Hu, L. Kou, and L. Sun, Sci. Rep. **6**, 31122 (2016).

[74] H.-L. Liu, C.-C. Shen, S.-H. Su, C.-L. Hsu, M.-Y. Li, and L.-J. Li, Appl. Phys. Lett. **105**, 201905 (2014).

[75] B. Scharf, T. Frank, M. Gmitra, J. Fabian, I. Žutić, and V. Perebeinos, Phys. Rev. B **94**, 245434 (2016).

[76] F. Wu, T. Lovorn, and A. H. MacDonald, Phys. Rev. B **97**, 035306 (2018).